Nature Communications

https://doi.org/10.1038/s41467-026-69536-4

Article in Press

Natural hyperbolicity of hexagonal boron nitride in the deep ultraviolet

Received: 13 December 2025

Accepted: 4 February 2026

Cite this article as: Choi, B., Lynch, J., Chen, W. *et al.* Natural hyperbolicity of hexagonal boron nitride in the deep ultraviolet. *Nat Commun* (2026). https://doi.org/10.1038/s41467-026-69536-4

Bongjun Choi, Jason Lynch, Wangleong Chen, Seong-Joon Jeon, Hyungseob Cho, Kyungmin Yang, Jonghwan Kim, Nader Engheta & Deep Jariwala

Natural Hyperbolicity of Hexagonal Boron Nitride in the Deep Ultraviolet

Bongjun Choi[1], Jason Lynch[1], Wangleong Chen[2], Seong-Joon Jeon[3,4], Hyungseob Cho[3,4], Kyungmin Yang[1], Jonghwan Kim[3,4,5]*, Nader Engheta[1,2,6,7]*, Deep Jariwala[1,2]*

[1]Department of Electrical and Systems Engineering, University of Pennsylvania, Philadelphia, Pennsylvania 19104, United States

[2]Department of Materials Science and Engineering, University of Pennsylvania, Philadelphia, Pennsylvania 19104, United States

[3]Department of Materials Science and Engineering, Pohang University of Science and Technology, Pohang, Republic of Korea.

[4]Center for van der Waals Quantum Solids, Institute for Basic Science (IBS), Pohang, Republic of Korea

[5]Department of Physics, Pohang University of Science and Technology, Pohang, Republic of Korea.

[6]Department of Bioengineering, University of Pennsylvania, Philadelphia, Pennsylvania 19104, United States

[7]Department of Physics and Astronomy, University of Pennsylvania, Philadelphia, Pennsylvania, 19104, United States

* Corresponding authors: dmj@seas.upenn.edu, engheta@seas.upenn.edu, jonghwankim@postech.ac.kr

Abstract

Hyperbolic media enable unique optical phenomena including hyperlensing, negative refraction, enhanced photonic density of states (PDOS), and highly confined polaritons. While most hyperbolic media are artificially engineered metamaterials, certain natural materials with extreme anisotropy can exhibit hyperbolic dispersion. Here, based on experimental evidence and theoretical fitting estimates to the experimental data, we suggest the presence of natural hyperbolic dispersion in hexagonal boron nitride (hBN) in the deep-ultraviolet (DUV) regime, induced by strong, anisotropic exciton resonances. Using all-optical imaging spectroscopic ellipsometry (ISE), we characterize the complex dielectric function along in-plane and out-of-plane directions down to 190 nm (6.53 eV), revealing a potential type-II hyperbolic window in the DUV regime. We predict that hyperbolicity supports hyperbolic exciton polaritons (HEP) with high directionality and slow group velocity, as confirmed by numerical calculations. Our findings suggest hBN as a platform for nanophotonic applications in the technologically significant DUV spectral range.

Introduction

Nanoscale light manipulation is crucial for developing next-generation nano-optical devices for sensing[1], waveguiding[2], and imaging[3]. Hyperbolic media, characterized by permittivities of opposite sign along different crystal axes (e.g., $Re(\varepsilon_{\parallel}) \times Re(\varepsilon_{\perp}) < 0$), have attracted significant attention due to their ability to support large wavevectors, enabling extreme sub-diffraction light confinement, and large photonic density of states (PDOS)[4,5]. Since hyperbolic dispersion requires large anisotropy, it is typically achieved in artificially made hyperbolic metamaterials (HMMs)[3,6-9], which are realized by subwavelength multilayer stacks of alternating dielectric and metallic films, exhibiting hyperbolic dispersion because it heavily relies on the plasmonic resonance of the metal layers[4]. These HMMs exhibit an open isofrequency surface, supporting the propagation of high-momentum waves and enabling unique phenomena like negative refraction[10], sub-diffraction imaging via hyperlensing[3,8,9], and substantial enhancement of the Purcell factor[11].

Van der Waals (vdW) two-dimensional (2D) materials exhibit inherent high anisotropy along the out-of-plane direction due to their layered structure. This pronounced anisotropy is a key prerequisite for hyperbolic dispersion[12-14]. Moreover, the pronounced anisotropy of certain vdW 2D crystals gives rise to strongly direction-dependent resonances—phonons, plasmons, and excitons—which profoundly impact their dielectric response[15]. With the discovery of vdW 2D crystals, hyperbolic dispersion can be more readily achieved, rather than relying on plasmonic multilayer HMMs. Prior results have revealed hyperbolic behavior originating from the anisotropic resonances of phonons in α-MoO_3[16] and hexagonal boron nitride (hBN)[17], plasmons in WTe_2[18], and excitons in monolayer black phosphorus (BP)[19] and chromium sulfide bromide (CrSBr)[20] at cryogenic temperatures, as well as in various 2D vdW heterostructures[2,21-23].

Natural hyperbolic media support hybrid electromagnetic modes (hyperbolic polaritons) that enable broadband, deeply sub-diffractional confinement with strongly directional propagation. Natural hyperbolic phonon polaritons were first observed in hBN crystals experimentally by near-field measurements in the mid-infrared (MIR)[24]. Since then, various hyperbolic polaritons driven by phonons[16,24], plasmons[25], and excitons[20] have been demonstrated across many material platforms. While phonon- and plasmon-mediated hyperbolicity has been extensively explored, exciton-induced hyperbolicity remains relatively rare, as it requires materials with exceptionally strong excitonic resonances with extreme anisotropy.

hBN is a well-known vdW polar dielectric exhibiting hyperbolic dispersion in the MIR regime due to anisotropic phonon resonances[15,24]. It has also attracted attention as an excitonic material due to its strong emission in the deep-ultraviolet (DUV) regime (around 180 ~ 300 nm, 4.13 ~ 6.89 eV)[26]. Even though the fundamental bandgap of hBN is an indirect bandgap (K→M point) in the DUV regime, as proved by the two-photon

excitation spectroscopy[27], it also has a direct transition near ~ 6.1 eV at the K valley, supported by numerous density-functional theory (DFT) calculations and experiments[28-30]. Strong in-plane covalent bonding and weak out-of-plane van der Waals interactions create tightly bound 2D excitons with the large binding energy, E_b ~700 meV, for the lowest exciton[28,31-33]. In addition, the electronic flatband of hBN in the Brillouin zone facilitates strong light-matter interaction[28].

We suggest the presence of natural hyperbolic dispersion in hBN, arising from its anisotropic strong exciton resonances in the DUV regime. Here, using imaging spectroscopic ellipsometry (ISE), we characterize the complex refractive index and exciton resonance properties of hBN along in-plane (∥) and out-of-plane (⊥) directions. hBN shows pronounced exciton oscillator strength in the in-plane direction compared to the out-of-plane direction, suggesting the presence of a hyperbolic window in the DUV regime. We predict that this hyperbolicity enables a transition in the isofrequency contour from elliptic (closed) to hyperbolic (open) shape[5], supporting hyperbolic exciton polaritons (HEP) with high directionality and confinement[15,20,34]. Our findings would enable light manipulation at the nanoscale in the DUV regime, which is critical for extreme-resolution photolithography using 193 nm ArF excimer lasers and DUV nonlinear optics.

Results and Discussion

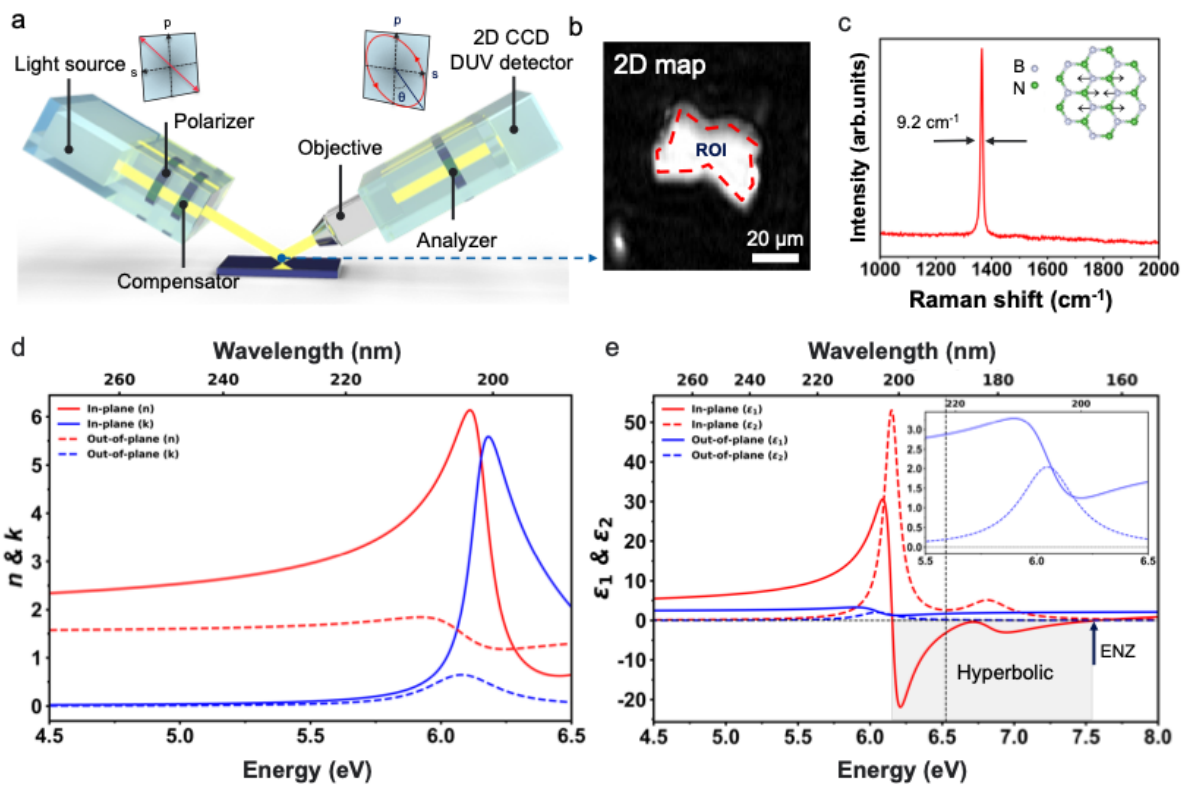

Figure 1. Imaging spectroscopic ellipsometry measurement of hexagonal boron nitride (hBN). (a) Schematic illustration of imaging spectroscopic ellipsometry (ISE). Unlike conventional spectroscopic ellipsometry, imaging ellipsometry uses a high-resolution (~1 μm) 2D charge-coupled device (CCD) detector with an objective lens (7×) to map Ψ and Δ values, allowing the

extraction of optical properties from even small flakes. (b) Example of the mapped image data of a small hBN flake using ISE. The red dashed outline indicates the region of interest (ROI). (c) Raman spectrum obtained from measured hBN shows a clear E_{2g} resonance with a narrow full width at half maximum (FWHM), demonstrating the high quality of the measured hBN. The inset shows a schematic illustration of the in-plane stretching mode of B and N atoms. (d) Refractive index (n) and extinction coefficient (k) of hBN along the different optical axes (in-plane (∥) and out-of-plane (⊥)) showing strong excitonic features of hBN. These extracted values from ISE are in agreement with prior measurements using synchrotron radiation and inelastic electron scattering[30,35]. (e) Complex permittivities ($\varepsilon = \varepsilon_1 + i\varepsilon_2$) of hBN along different optical axes (in-plane (∥) and out-of-plane (⊥)) indicating apparent hyperbolic dispersion (grey shaded area) in the deep-ultraviolet (DUV) regime with epsilon-near-zero (ENZ) point. The permittivities are extrapolated based on the multiple Lorentz oscillator model obtained from the ISE measurement above (below) 6.53 eV (190 nm). The dashed vertical line represents the boundary between the experimental and extrapolated regimes. The inset presents a magnified view of the out-of-plane complex permittivity in the excitonic regime near 6.05 eV. All complex refractive indices are listed in the Supplementary Table 1.

While hBN's optical properties in the DUV have been widely studied, most prior studies have focused on its electronic band structure calculation from the *ab initio* approach and its interband transitions by inelastic electron scattering (IES) measurement[28,30,32,36]. In contrast, spectroscopic ellipsometry studies, which provide direct and sensitive optical characterization in the DUV regime, remain scarce[14,35]. Particularly, refractive indices resolved separately along the in-plane and out-of-plane directions are rare, yet they provide indispensable insight into the material's anisotropy and hyperbolic nature in the DUV excitonic regime. Recent ellipsometry studies have revealed a high refractive index and strong birefringence of hBN in the UV regime (around 250 nm), although they did not capture the excitonic resonance in the DUV regime[14]. We first characterize the excitonic features and refractive index of hBN along in-plane (∥) and out-of-plane (⊥) directions using ISE down to the DUV to NIR regimes (190 ~ 1000 nm, 1.24 ~ 6.53 eV). First, we prepare the hBN sample using mechanical exfoliation with tape and transfer it onto the target substrate (See Methods). We chose c-plane Al_2O_3 as the substrate, which has a wide bandgap to increase the reflectance in the DUV regime. Since the excitonic resonances of hBN occur in the DUV range, where most materials (e.g., Si) strongly absorb light, using an Al_2O_3 substrate minimizes absorption and enhances the reflected light intensity (Supplementary Figure 1). When linearly polarized light is incident on a sample, strong excitonic resonances in its dielectric function cause variations in the Fresnel reflection coefficients r_p and r_s, consequently changing the ellipsometry parameters Ψ (the amplitude ratio) and Δ (the phase difference) with high sensitivity, enabling exciton behavior characterization[37]. Furthermore, obliquely incident light distinguishes a sample's electromagnetic response parallel to the surface from that perpendicular to it (Figure 1a)[37]. As shown in Figure 1b, an exfoliated hBN flake was characterized by ISE. The ~ 1 μm lateral resolution of our ISE allows detailed optical properties (Ψ and Δ) map data to be acquired as a function of incidence angle and wavelength on the small flakes that are inaccessible with conventional spectroscopic ellipsometry. The Raman spectrum of hBN exhibits a sharp peak at 1370 cm^{-1}, the characteristic E_{2g} vibrational mode, corresponding to the in-plane stretching of B and N atoms, as illustrated in the inset (Figure 1c)[31]. The narrow peak with a full width at half maximum (FWHM) of approximately 9.2 cm^{-1} (~8 cm^{-1} for flux grown and ~30 cm^{-1} for

MOCVD) indicates that the hBN possesses high crystalline quality with minimal structural disorder and low strain, both of which are essential for sustaining strong excitonic resonances[38,39]. We obtain the Ψ and Δ (Supplementary Figure 2) map and make the optical model using multiple Lorentz oscillator models to capture the exciton resonance behavior in hBN (see Supplementary Note 1)[37,40-45]. We use phenomenologically extracted parameters from ellipsometry because they provide a convenient and reliable basis for the Lorentz model, avoiding the need for direct measurements of radiative and non-radiative rates. Because hBN is an uniaxial material, we modelled the in-plane and out-of-plane dielectric functions independently using distinct multiple Lorentz oscillator models. To improve the reliability of the results, multiple hBN thicknesses are measured at various incidence angles between 40° and 70° with respect to the sample's surface. The large variation in incidence angle, and thick flakes, yields a strong out-of-plane signal allowing us to determine the uniaxial dielectric function with high fidelity. The multiple Lorentz oscillator model captures the interband transitions in hBN along different optical axes with high accuracy, showing strong agreement with the experimentally obtained Ψ and Δ values across various incident angles and hBN thicknesses (Supplementary Figure 3).

The measured hBN's complex refractive index is shown in Figure 1d along the in-plane ($\parallel$) and out-of-plane ($\perp$) directions. In the in-plane direction, hBN exhibits a pronounced excitonic resonance near 6.14 eV, characterized by a large extinction coefficient (k), which arises from the direct $\pi \rightarrow \pi^*$ transition at the K point in the reciprocal space. This observation aligns well with the theoretical electronic band calculation using the *ab initio* (GW+BSE) method[28,32] as well as prior experimental measurements using synchrotron radiation[35] and inelastic electron scattering[30]. Although bulk hBN possesses an indirect bandgap, phonon-assisted (indirect) optical transitions are essentially absent from the measured spectra since their oscillator strength is orders of magnitude weaker than that of the dominant excitonic resonance[46,47]. Furthermore, hBN exhibits a high refractive index (~2.5 at 250 nm) in the UV regime due to strong excitonic resonances. These characteristics make hBN an attractive high-index material alternative to conventional low-index UV materials such as fused silica (SiO_2, n ~1.5 at 250 nm)[48] and magnesium fluoride (MgF_2, n ~ 1.4 at 250 nm)[49]. On the other hand, hBN exhibits the interband transition along the out-of-plane direction approximately at 6.05 eV with a small extinction coefficient (*k*) compared to that of the in-plane components due to its highly in-plane oriented exciton nature[31]. This observation is well aligned with the previous literature[30], manifesting strong and anisotropic excitonic behavior, which induces hyperbolic dispersion, discussed later. As shown in Figure 1e, we plot the complex permittivity ($\varepsilon = \varepsilon_1 + i\varepsilon_2$) of hBN, where $\varepsilon_1 = n^2 - k^2$ and $\varepsilon_2 = 2nk$, along both its in-plane and out-of-plane directions. The permittivity was directly retrieved from ISE measurements down to 190 nm (6.53 eV), a measurable wavelength regime from our tool. To extend our model to shorter wavelengths ($\sim$155 nm, ~8.0 eV), we extrapolated the data using a multi Lorentz oscillator model (See Supplementary Note 1) obtained from multiple samples and incidence angles. Since the higher energy electron transition above 6.53 eV is out of range from our tool, we adapted the previous synchrotron study to capture the high energy interband transitions (e.g., $\pi \rightarrow \pi^*$ transition (~ 6.14 and 6.82 eV) and $\sigma \rightarrow \sigma^*$ transition (~15 eV))[35]. Due to its pronounced anisotropic excitonic resonances, we suggest that

hBN supports a well-defined DUV type-II hyperbolic window around 6.17 eV ~ 7.56 eV (164 nm ~ 201 nm), where $\varepsilon_{1,\parallel} < 0$ and $\varepsilon_{1,\perp} > 0$. We further identify an intrinsic epsilon-near-zero (ENZ) wavelength in hBN near 7.56 eV, where the losses are minimal. These naturally occurring hyperbolicity and ENZ points promise new opportunities for DUV nanophotonic device engineering and quantum-optical applications[50,51]

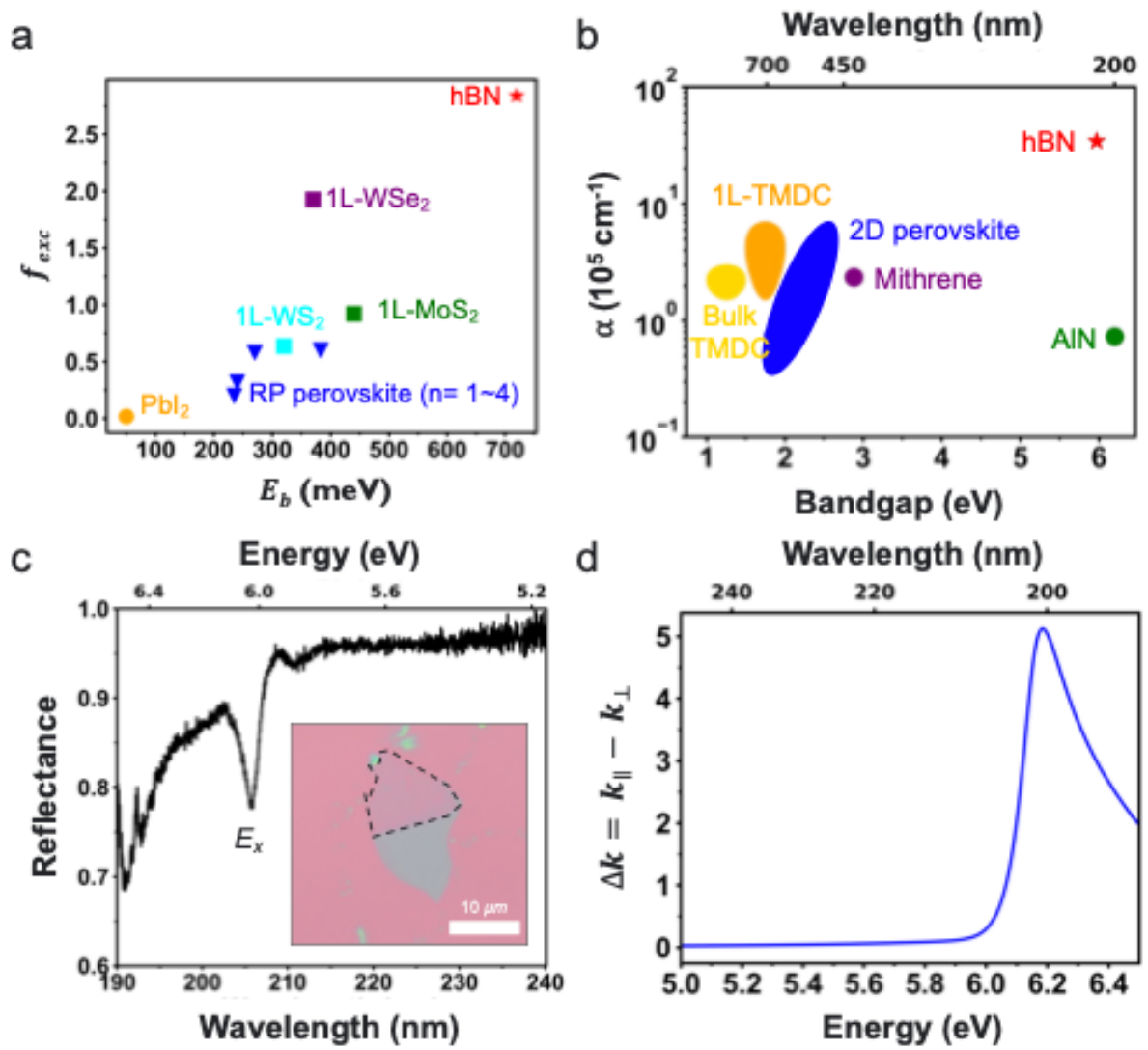

Figure 2. Exciton properties of hBN. (a) Comparison of exciton oscillator strength and exciton binding energy of various excitonic materials (hBN[32], monolayer transition metal dichalcogenides (TMDCs)[19,52-54], 2D Ruddlesden-Popper (RP) perovskite[55,56], and PbI_2[57]), showing hBN's strong oscillator strength and exciton binding energy compared to the other excitonic materials. The exciton oscillator strengths are calculated using Eq. (1), and parameters such as interband oscillator strength, Bohr radius, and E_b are adapted from prior literature[19,32,52-57]. (b) Comparison of the absorption coefficient along the in-plane directions of various excitonic (hBN, Bulk and monolayer of TMDCs (MoS_2, $MoSe_2$, $MoTe_2$, WSe_2, and WS_2), 2D RP and Dion-Jacobson (DJ) perovskites, mithrene, and AlN)[56,58-62], illustrating significant absorption coefficient due to the tightly bound excitons in hBN (c) Reflectance spectrum (R_{hBN}/R_{Al}) in a 5L-hBN/Al structure,

demonstrating the high absorbance from the thin hBN layer due to strong exciton resonance. The Al substrate serves as a back reflector, enhancing the excitonic absorption. The reflectance dips around 190 nm (6.53 eV) are originated from strong absorption of air. Inset shows image of thin hBN flake on a Si/SiO_2 substrate before the pick-up transfer. Note that the thickness of hBN was determined by the ISE measurement (Supplementary Figure 5) (d) Calculated linear dichroism ($\Delta k = k_{\parallel} - k_{\perp}$) as a function of photon energy, revealing a large dichroism originated from anisotropic exciton resonances.

Since excitonic resonances play a critical role in determining the optical properties—such as the dielectric functions and potential hyperbolic dispersion—of 2D excitonic materials, we investigate the excitonic feature of hBN to analyze the origin of hyperbolicity by evaluating its exciton oscillator strength from the interband oscillator strength in ellipsometry measurements (Figure 2a). Generally, because 2D materials strongly support confined excitons in two dimensions with reduced dielectric screening, they exhibit significantly larger E_b and strong oscillator strengths compared to their bulk counterparts[63]. The exciton oscillator strengths (f_{exc}) can be calculated using the simple formulation proposed by *Ishihara et al.*[57].

$$f_{exc} = \frac{2fS_0}{\pi a_{2D}^2} \; or \; \frac{2fV_0}{\pi a_{3D}^2} \tag{1}$$

, where f is the interband oscillator strength, S_0 (V_0) is a unit-cell area (volume), and $a_{2D\,(3D)}$ is the material's 2D (3D) Bohr radius. Since a smaller exciton Bohr radius is advantageous for the strong oscillator strength, f_{exc} shows an inversely square (cubic) proportional relation to Bohr radius, respectively. Tightly bound hBN excitons exhibit a small Bohr radius[31], resulting in a pronounced f_{exc} and E_b compared to the well-known highly excitonic materials, such as monolayer transition metal dichalcogenides (TMDCs), and 2D Ruddlesden-Popper (RP) perovskites. Monolayer TMDCs exhibit a large oscillator strength, although it is slightly smaller than that of hBN. The oscillator strength can increase at low temperatures, where excitons become more stable and nonradiative broadening is suppressed. Consequently, several studies have reported hyperbolic dispersion of 2D vdW materials (e.g., BP and CrSBr) at low temperatures, where excitonic resonances are enhanced, highlighting the critical role of excitons in governing hyperbolicity[19,20,64]. Furthermore, RP perovskites exhibit a near-hyperbolic dispersion around exciton resonance, characterized by $Re(\varepsilon_{\parallel})$ approaching zero while $Re(\varepsilon_{\perp})$ remains positive, suggesting that true hyperbolicity could potentially emerge at low temperatures[56]. For comparison, PbI_2, which does not support strong excitonic effects, exhibits small values of f_{exc} and E_b, indicating that excitons play an important role in the material's optical properties[57]. Figure 2b shows the absorption coefficient, $\alpha = 4\pi k/\lambda$, of various well-known excitonic materials including hBN (Bulk and monolayer TMDCs, 2D RP and Dion-Jacobson (DJ) perovskites, mithrene (AgSePh), and AlN). The giant excitonic oscillator strength of hBN enables a strong absorption peak around the exciton energy approximately $3.5 \times 10^6\, cm^{-1}$ (Supplementary Figure 4), which is consistent with the observation in Figure 2a. Because exciton oscillator strength scales with optical absorption, monolayer TMDCs, where reduced dielectric screening enhances excitonic

features such as E_b and f_{exc} ,exhibit more significant absorption coefficients than their bulk counterparts. Notably, hBN's tightly bound exciton gives rise to absorption coefficients nearly an order of magnitude higher than other excitonic semiconductors. Even compared to wide-bandgap AlN, whose band edge lies similarly in the DUV, hBN's excitonic resonance boosts its absorption by approximately two orders of magnitude, underscoring the dramatic impact of its bound excitons. Therefore, exciton dominates the optical responses in the DUV regime of hBN.

To probe the strong excitonic response, we measure the reflectance spectrum of thin hBN (5 layers) on an Al substrate in the DUV regime. The spectrum reveals pronounced absorption near the exciton energy even from a very thin hBN layer, as shown in Figure 2c. Notably, most of the observed absorption originates from the hBN layer rather than the underlying Al substrate, and the exciton resonance exhibits a slight shift from its intrinsic energy as a result of phase accumulation across the layer[65], as confirmed by the transfer matrix method (TMM)[66,67] calculation results (Supplementary Figure 6). More importantly, these strong excitons only exist along the in-plane direction, resulting in a large dichroism ($\Delta k = k_{\parallel} - k_{\perp}$) around 5, which reflects the difference in absorption properties along different optical axes, a prerequisite for natural hyperbolicity. Along with dichroism, hBN shows large birefringence in the DUV regime since dichroism and birefringence are related under the Kramers-Kronig relation (Supplementary Figure 7)[37]. In addition, the large birefringence of hBN, even well below the band gap where loss is low, makes it uniquely suited for UV and DUV polarization optics; an attribute few other materials can match[14].

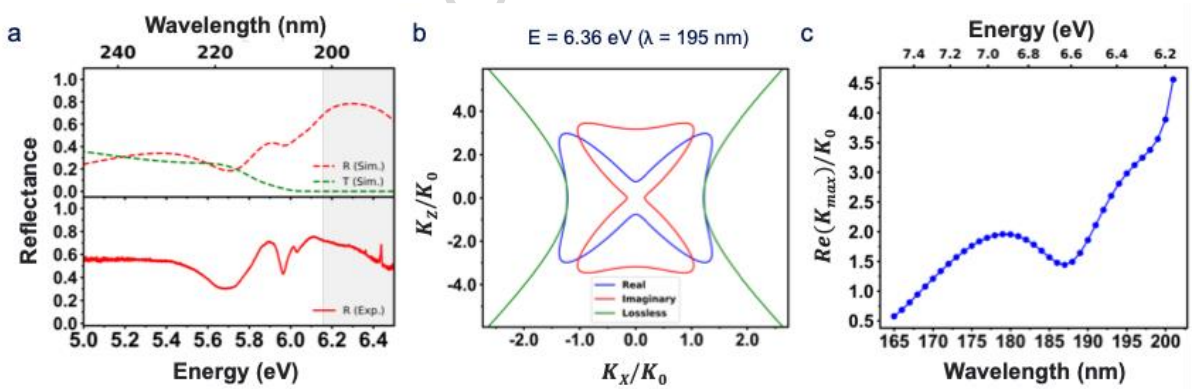

Figure 3. Natural hyperbolic dispersion in hBN. (a) Measured (solid red curve, bottom panel) and simulated (dotted red curve, top panel) reflectance, along with simulated transmittance (dotted green curve, top panel), from a 63 nm hBN sample on a c-plane Al_2O_3 substrate in the DUV regime, showing the highly reflective plateau (grey shaded area) associated with the hyperbolicity. (b) Isofrequency surface of hBN at 6.36 eV (195 nm) for transverse-magnetic (TM) plane wave with real loss (red and blue curves) and no loss (green curve), showing clear hyperbolic dispersion attributed to different signs of permittivities along different optical axes. (c) The max wavevector can be supported by the hBN as a function of wavelength (photon energy), reaching approximately ~4.6 around the exciton resonance.

In its type-II hyperbolic regime (6.17 eV ~ 7.56 eV), hBN exhibits a metallic in-plane permittivity while maintaining a dielectric response along the out-of-plane direction, a

characteristic feature of type-II hyperbolic materials, and shows a highly reflective plateau in the hyperbolic regime. Our measured and simulated reflectance spectrum from hBN (63 nm) on Al_2O_3 substrate exhibit the high reflectivity plateau of the hBN (grey-shaded region), a consequence of its hyperbolic dispersion (Figure 3a)[17,28]. The highly reflective plateau is observed in hBN flakes of various thicknesses (see Supplementary Figure 8a). Note that we chose an hBN thickness exceeding approximately 20 nm, where hBN exhibits highly reflective behavior due to coherent radiative decay, as confirmed by the TMM calculation shown in Supplementary Figure 8b. As hBN approaches the optically thin limit, strong excitonic damping becomes dominant. This causes the broad plateau to evolve into a single resonance peak, consistent with the observation in Figure 2c and analogous to the phononic Reststrahlen band in the mid-infrared (MIR) regime of hBN[23,68]. In addition, the simulated transmission spectrum dips to near zero, confirming that electromagnetic waves cannot propagate normally through the hBN in this band except as evanescent/high-k modes as shown in Figure 3a. The reflective plateau exhibits a highly reflective nature across a wide range of incident angles in the hyperbolic regime (Supplementary Figure 8c).

The hyperbolic features are manifested only under transverse-magnetic (TM)-polarized light, as it probes both in-plane and out-of-plane dielectric responses. In contrast, transverse-electric (TE)-polarized light is sensitive only to the in-plane permittivity and may not exhibit hyperbolic behavior. For the TM plane wave, Maxwell's equation yields a dispersion relation: $\frac{k_x^2}{\varepsilon_{1,\perp}} + \frac{k_z^2}{\varepsilon_{1,\parallel}} = k_0^2$, where $k_0 = \frac{\omega}{c}$ is the free space wavevector, and k_x and k_z are the wavevectors in the x-plane and z-plane, respectively. Based on the dispersion relation, Figure 3b shows the clear hyperbolic isofrequency surface of hBN at 6.36 eV (195 nm) for each lossy (red and blue) and lossless (green) case, while hBN exhibits an elliptical dispersion outside the hyperbolic region as expected (Supplementary Figure 9). The anisotropic excitonic resonance suggests the possibility of a hyperbolic dispersion, supporting highly confined light and large PDOS, enabling the formation of hyperbolic polaritons discussed later[15,20,69]. In an ideal, lossless hyperbolic medium, the dispersion relation admits modes with infinitely large wavevectors in theory, formally yielding an infinite PDOS. In practice, however, material absorption introduces damping that imposes a finite cutoff on the maximum supported k-vector, resulting in a closed isofrequency surface[70], as shown in Figure 3b. Thus, it becomes essential to quantify the impact of absorption, especially in regimes where hyperbolic dispersion is driven by exciton resonances, since these same resonances impart strong intrinsic damping. Over hBN's hyperbolic band, we compute the largest wavevector the material can support as a function of photon energy (wavelength). Approaching the exciton resonance, hBN's hyperbolic bands extend to larger wavevectors, albeit with rising absorption. Supplementary Figure 10 compares the loss-inclusive isofrequency contours at multiple photon energies (wavelength): as one approaches the exciton resonance ($\sim$6.14 eV), the real isofrequency surface expands (indicating larger wavevector) while the imaginary isofrequency surface grows simultaneously, indicating increased damping near the resonance. In its most extreme hyperbolic regime, hBN reaches $\mathrm{Re}(K_{max})/K_0 \sim$ 4.6 (Figure 3c). Additionally, the enlarged wavevector space within hBN's hyperbolic band significantly enhances the PDOS, which is calculated by the Green's functions, resulting

in an enhanced spontaneous emission rate, as quantified by the Purcell factor shown in the Supplementary Figure 11 [4,71].

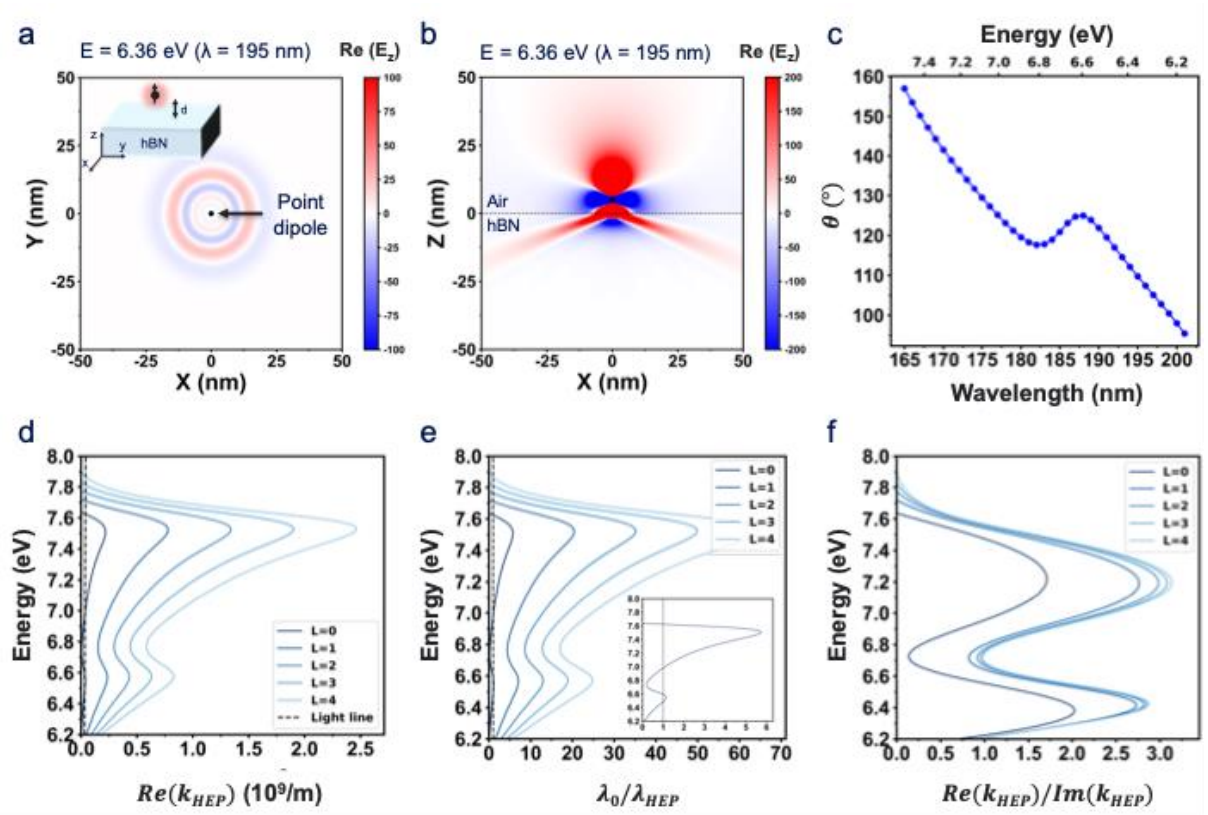

Figure 4. Hyperbolic exciton polaritons (HEP) propagation in hBN slab. Numerically simulated near-field wave propagation at 6.36 eV (195 nm) using finite-difference time-domain (FDTD) simulations, launched by a point dipole located above the hBN slab (d = 5 nm) and oriented along the Z-axis, is shown in (a) the in-plane (XY) direction, revealing isotropic and radial propagation, and (b) the out-of-plane (XZ) direction, exhibiting the highly directional wave propagation in the hBN layer (Z<0) associated with the hyperbolic dispersion, unlike the air (Z>0). (c) Wave propagation angle as a function of photon energy (wavelength). (d) The HEP's analytical dispersion relation as a function of an in-plane wavevector up to L=4 mode, where d_{hBN} is 10 nm, showing the highly confined nature of HEP. Calculated figure of merits: (e) Confinement factor (λ_0/λ_{HEP}, inset shows zoomed-in L=0 mode) and (f) Propagation loss properties ($Re(k_{HEP})/Im(k_{HEP})$) of HEP as a function of incident photon energy, showing highly confined propagation characteristic.

We further investigate the highly confined HEP associated with the hyperbolic dispersion. The numerically simulated wave launched by a point source oriented along the z-axis, as illustrated in the inset of Figure 4a, displays a circularly shaped radial wave propagation at 6.36 eV (195 nm) in the XY plane. Since radiation in the XY plane consists solely of the E_z component, governed exclusively by a positive $\varepsilon_\perp$, the resulting radiation pattern exhibits the symmetric propagation shown in Figure 4a. In contrast, the radiation pattern in the XZ plane comprises two components (E_x and E_z), allowing the field to probe the hyperbolic dispersion. Consequently, a point source positioned above a type-II hyperbolic medium (Z<0) produces a sharply defined hyperbolic radiating pattern in the XZ planes

(Figure 4b), which is consistent with the isofrequency surface at 6.36 eV (195 nm) in reciprocal space in Figure 3b. On the other hand, the point source launched at 4.96 eV (250 nm), which is outside of the hyperbolic window, does not show directional propagation as can be expected from its isofrequency contour (Supplementary Figure 12). Since HEP supports large momentum, they are difficult to excite via direct free-space incidence in the far field[1]. Thus, using a high-index prism such as the Otto and Kretschmann configuration under TM-polarized illumination enables efficient coupling to these high-k modes (Supplementary Figure 13)[72].

This hyperbolic dispersion enables highly directional propagation in the XY and XZ planes for type-I and II, respectively, and leads to strong electric field confinement of HEP in the near field, in contrast to elliptical dispersion materials where energy spreads across all planes[15,73]. In addition, HEP exhibits directional propagation depending on the frequency, and the propagation angle (θ), the angle between the Poynting vector and the z axis, can be approximately calculated by Eq. (2)[34]:

$$\theta(\omega) = \pi/2 - \tan^{-1}(\sqrt{\varepsilon_{\perp}(\omega)}/i\sqrt{\varepsilon_{\parallel}(\omega)}) \quad (2)$$

In this regime, polaritons can only propagate at specific angles determined by the anisotropy of the material. The propagation angle (θ) decreases from 157° to 95° (Δθ ≅ 62°) within the hyperbolic window as photon energy decrease (wavelength increases) (Figure 4c). Simulated wave propagation in the XZ plane as a function of photon energy exhibits pronounced directionality, in agreement with the calculations shown in Figure 4c. (Supplementary Figure 14). We analytically solve the HEP dispersion relation for TM modes, in the thin hBN slab following the general equations for the TM polariton mode given by Eq. (3)[74]:

$$k_{HEP} = \frac{i}{d_{hBN}}\sqrt{\frac{\varepsilon_{\perp}}{\varepsilon_{\parallel}}}\left[2\tan^{-1}\left(i\frac{1}{\sqrt{\varepsilon_{\perp}\varepsilon_{\parallel}}}\right) + \pi L\right] \quad (3)$$

, where k_{HEP} is the x component of the wavenumber, d_{hBN} is the thickness of the hBN slab and L = 0, 1, 2 … are integers indicating the higher order mode. The analytical dispersion relation derived from Eq. (3) clearly reveals the HEP mode, which carries a larger momentum than that of a free-space photon, where the dashed line represents the light line (Figure 4d). As expected for the hyperbolic polariton, the HEP's dispersion relation exhibits an increasing momentum as mode order increases. In addition, the group velocity ($v_g = \partial\omega/\partial k_{HEP}$), the slope of the dispersion curve, decreases with increasing momentum, reflecting the slow group velocity and strong spatial confinement of higher-order modes[17]. We extract the commonly used figure of merits for the polariton: the confinement factor (λ_0/λ_{HEP}) ,where λ_0 is the free-space wavelength, and propagation figure of merit of HEP, defined as $Re(k_{HEP})/Im(k_{HEP})$ [69,75]. Figure 4e shows the confinement factor depending on the mode order, showing the highly confined nature of HEP with an increase in confinement as the mode order increases. For the L=0 mode, the confinement factor reaches approximately 5.7, which is comparable to the values observed in exciton-polaritons in WSe_2 (Figure 4e inset)[76]. In addition, the confinement

factor reaches values exceeding 10 for higher-order modes, underscoring the extreme subwavelength confinement enabled by the hyperbolic dispersion in hBN. As shown in Figure 4f, higher propagation figure of merit values indicates reduced relative propagation losses of HEP. This suggests that, despite their inherently large momentum, HEP can still propagate appreciable distance (~20 nm) before significant attenuation occurs[64,74]. Furthermore, the value of propagation figure of merit increases with mode order, reflecting improved loss-performance characteristics in higher-order modes. The calculated propagation length along the direction corresponding to the maximum real part of the wavevector is approximately 20 nm (Supplementary Figure 15a)[70]. In addition, the calculated HEP lifetime is approximately 0.1 fs, which is comparable to the values for HEP in hBN/WS_2/hBN heterostructures[74] (Supplementary Figure 15b).

In conclusion, from the spectroscopic ellipsometry analysis, we infer the emergence of natural hyperbolic dispersion in hBN arising from strong and anisotropic excitonic resonances in the DUV regime. Using ISE with micron resolution, we extract the complex dielectric functions along both in-plane and out-of-plane directions, revealing a clear type-II hyperbolic window induced by excitonic anisotropy. We associate the highly reflective plateau with hyperbolicity through reflectance spectroscopy, showing good agreement with numerical calculations. Moreover, we suggest that this hyperbolic dispersion supports highly confined polaritonic modes with large momenta, slow group velocities, and enhanced PDOS. Numerical simulations and analytical modeling of the HEP dispersion relation show strong confinement factors and moderate propagation figures of merit. These findings suggest hBN as a candidate for DUV nanophotonics, providing a pathway toward next-generation polaritonic devices for sub-diffraction imaging, DUV lithography, and quantum optical applications.

Methods

Sample preparation

The exfoliated hBN sample has prepared using two methods, direct transfer and pick-up transfer. For the direct transfer, the bulk hBN was exfoliated using blue tape and then directly dry transferred on top of the target substrate. For the pick-up transfer, mechanically exfoliated hBN flakes were picked up using a dry transfer method[77] with polycarbonate (PC) /polydimethylsiloxane (PDMS) and subsequently transferred onto the target substrate. After the transfer, the samples were immersed in chloroform for 1 hour to dissolve the PC film.

Imaging spectroscopic ellipsometry

Imaging ellipsometry measurements for determining the dielectric function were performed using the Accurion EP4 system (Park Systems) over the 190–1000 nm spectral range. A 7× objective lens was used for measurements in the DUV regime. Multi-angle incidence measurements were conducted over an angular range of 40° to 70°. The measured mapping data were analyzed using the EP4 model and DataStudio software provided by the EP4 system.

Raman characterization

Raman spectra were acquired using a Horiba LabRam HR Evolution confocal microscope, with a 600 grooves/mm grating and a 633 nm continuous-wave (CW) laser for excitation. The signal was detected using a CCD detector.

Reflectance measurements

Reflectance measurements were performed using a Hamamatsu deuterium lamp as the light source. The DUV light was guided into a home-built confocal microscopy set-up, which was constructed using DUV-enhanced aluminum mirrors, a DUV-enhanced reflective objective with a numerical aperture of 0.4, CaF_2 lenses, and a CaF_2 beam splitter. A 4f optical system was implemented, and a size-tunable aperture was placed at the image plane to spatially filter the reflected signal, thereby isolating the reflectance from the hexagonal boron nitride samples while blocking contributions from the underlying substrate. The reflected light was guided into a spectrometer and detected using an electrically cooled Si CCD camera.

Optical simulations

Electric field profiles in the near field were calculated using FDTD simulations performed with the commercial software Lumerical. Theoretical reflectance and absorbance are computed using the TMM with homemade Python code[66,67]. The refractive index of hBN was determined through imaging ellipsometry, while those of Al_2O_3[78] and Al[79] were adopted from previously reported literature values.

Data availability

Relevant data supporting the key findings of this study are available within the article and the Supplementary Information file. All raw data generated during the current study are available from the corresponding authors upon request.

Acknowledgement

D. J., B.C., and J.L. acknowledge support from the Office of Naval Research Young Investigator Award, Metamaterials Program (N00014-23-1-2037). This work was carried out in part at the Singh Center for Nanotechnology, which is supported by the NSF National Nanotechnology Coordinated Infrastructure Program under Grant NNCI-2025608. J.K. acknowledges the support from the Institute for Basic Science (IBS), Korea under Project Code IBS-R014-A1 and the National Research Foundation of Korea grants (NRF-2023R1A2C2007998). N. E. acknowledges partial support from the US Air Force Office of Scientific Research (AFOSR) Multidisciplinary University Research Initiatives (MURI) program with grant # FA9550-21-1-0312 and AFOSR grant # FA9550-23-1-030.7

Author Contribution

D.J. supervised and acquired funding for the project. D.J. and B.C. conceived and designed the experiment. B.C. performed the ellipsometry measurements and conducted the data fitting. B.C. performed the optical simulations and calculations in discussion with D.J., N.E., and J.L. W.C. fit preliminary ellipsometry data. K.Y. fabricated samples. S. J. and H.C. performed the reflectance measurement under the supervision of J. K. B.C. and

D.J. wrote the manuscript with inputs from all authors. All authors discussed the results and revised the manuscript.

Competing Interests

The authors declare no competing interests.

Figure Legends/Captions

Figure 1. Imaging spectroscopic ellipsometry measurement of hexagonal boron nitride (hBN). (a) Schematic illustration of imaging spectroscopic ellipsometry (ISE). Unlike conventional spectroscopic ellipsometry, imaging ellipsometry uses a high-resolution (~1 μm) 2D charge-coupled device (CCD) detector with an objective lens (7×) to map Ψ and Δ values, allowing the extraction of optical properties from even small flakes. (b) Example of the mapped image data of a small hBN flake using ISE. The red dashed outline indicates the region of interest (ROI). (c) Raman spectrum obtained from measured hBN shows a clear E_{2g} resonance with a narrow full width at half maximum (FWHM), demonstrating the high quality of the measured hBN. The inset shows a schematic illustration of the in-plane stretching mode of B and N atoms. (d) Refractive index (n) and extinction coefficient (k) of hBN along the different optical axes (in-plane (∥) and out-of-plane (⊥)) showing strong excitonic features of hBN. These extracted values from ISE are in agreement with prior measurements using synchrotron radiation and inelastic electron scattering[30,35]. (e) Complex permittivities ($\varepsilon = \varepsilon_1 + i\varepsilon_2$) of hBN along different optical axes (in-plane (∥) and out-of-plane (⊥)) indicating apparent hyperbolic dispersion (grey shaded area) in the deep-ultraviolet (DUV) regime with epsilon-near-zero (ENZ) point. The permittivities are extrapolated based on the multiple Lorentz oscillator model obtained from the ISE measurement above (below) 6.53 eV (190 nm). The dashed vertical line represents the boundary between the experimental and extrapolated regimes. The inset presents a magnified view of the out-of-plane complex permittivity in the excitonic regime near 6.05 eV. All complex refractive indices are listed in the Supplementary Table 1.

Figure 2. Exciton properties of hBN. (a) Comparison of exciton oscillator strength and exciton binding energy of various excitonic materials (hBN[32], monolayer transition metal dichalcogenides (TMDCs)[19,52-54], 2D Ruddlesden-Popper (RP) perovskite[55,56], and PbI_2[57]), showing hBN's strong oscillator strength and exciton binding energy compared to the other excitonic materials. The exciton oscillator strengths are calculated using Eq. (1), and parameters such as interband oscillator strength, Bohr radius, and E_b are adapted from prior literature[19,32,52-57]. (b) Comparison of the absorption coefficient along the in-plane directions of various excitonic (hBN, Bulk and monolayer of TMDCs (MoS_2, $MoSe_2$, $MoTe_2$, WSe_2, and WS_2), 2D RP and Dion-Jacobson (DJ) perovskites, mithrene, and AlN)[56,58-62], illustrating significant absorption coefficient due to the tightly bound excitons in hBN (c) Reflectance spectrum (R_{hBN}/R_{Al}) in a 5L-hBN/Al structure, demonstrating the high absorbance from the thin hBN layer due to strong exciton resonance. The Al substrate serves as a back reflector, enhancing the excitonic absorption. The reflectance dips around 190 nm (6.53 eV) are originated from strong absorption of air. Inset shows image of thin hBN flake on a Si/SiO_2 substrate before the pick-up transfer. Note that the thickness of hBN was determined by the ISE measurement (Supplementary Figure 5) (d) Calculated linear dichroism ($\Delta k = k_{\parallel} - k_{\perp}$) as a function of photon energy, revealing a large dichroism originated from anisotropic exciton resonances.

Figure 3. Natural hyperbolic dispersion in hBN. (a) Measured (solid red curve, bottom panel) and simulated (dotted red curve, top panel) reflectance, along with simulated transmittance (dotted green curve, top panel), from a 63 nm hBN sample on a c-plane Al_2O_3 substrate in the DUV regime, showing the highly reflective plateau (grey shaded area) associated with the hyperbolicity. (b) Isofrequency surface of hBN at 6.36 eV (195 nm) for transverse-magnetic (TM) plane wave with real loss (red and blue curves) and no loss (green curve), showing clear hyperbolic dispersion attributed to different signs of permittivities along different optical axes. (c) The max wavevector can be supported by the hBN as a function of wavelength (photon energy), reaching approximately ~4.6 around the exciton resonance.

Figure 4. Hyperbolic exciton polaritons (HEP) propagation in hBN slab. Numerically simulated near-field wave propagation at 6.36 eV (195 nm) using finite-difference time-domain (FDTD) simulations, launched by a point dipole located above the hBN slab (d = 5 nm) and oriented along the Z-axis, is shown in (a) the in-plane (XY) direction, revealing isotropic and radial propagation, and (b) the out-of-plane (XZ) direction, exhibiting the highly directional wave propagation in the hBN layer (Z<0) associated with the hyperbolic dispersion, unlike the air (Z>0). (c) Wave propagation angle as a function of photon energy (wavelength). (d) The HEP's analytical dispersion relation as a function of an in-plane wavevector up to L=4 mode, where d_{hBN} is 10 nm, showing the highly confined nature of HEP. Calculated figure of merits: (e) Confinement factor (λ_0/λ_{HEP}, inset shows zoomed-in L=0 mode) and (f) Propagation loss properties ($Re(k_{HEP})/Im(k_{HEP})$) of HEP as a function of incident photon energy, showing highly confined propagation characteristic.

References

1 Sreekanth, K. V. *et al.* Extreme sensitivity biosensing platform based on hyperbolic metamaterials. *Nature materials* **15**, 621-627 (2016).

2 Sternbach, A. *et al.* Programmable hyperbolic polaritons in van der Waals semiconductors. *Science* **371**, 617-620 (2021).

3 Liu, Z., Lee, H., Xiong, Y., Sun, C. & Zhang, X. Far-field optical hyperlens magnifying sub-diffraction-limited objects. *science* **315**, 1686-1686 (2007).

4 Poddubny, A., Iorsh, I., Belov, P. & Kivshar, Y. Hyperbolic metamaterials. *Nature photonics* **7**, 948-957 (2013).

5 Krishnamoorthy, H. N., Jacob, Z., Narimanov, E., Kretzschmar, I. & Menon, V. M. Topological transitions in metamaterials. *Science* **336**, 205-209 (2012).

6 Yang, X., Yao, J., Rho, J., Yin, X. & Zhang, X. Experimental realization of three-dimensional indefinite cavities at the nanoscale with anomalous scaling laws. *Nature Photonics* **6**, 450-454 (2012).

7 Lynch, J. *et al.* High-temperature-resilient hyperbolicity in a mixed-dimensional superlattice. *Matter* **8**, 102290 (2025). https://doi.org:https://doi.org/10.1016/j.matt.2025.102290

8 Salandrino, A. & Engheta, N. Far-field subdiffraction optical microscopy using metamaterial crystals: Theory and simulations. *Physical Review B—Condensed Matter and Materials Physics* **74**, 075103 (2006).

9 Jacob, Z., Alekseyev, L. V. & Narimanov, E. Optical hyperlens: far-field imaging beyond the diffraction limit. *Optics express* **14**, 8247-8256 (2006).

10 Hoffman, A. J. *et al.* Negative refraction in semiconductor metamaterials. *Nature materials* **6**, 946-950 (2007).

11 Poddubny, A. N., Belov, P. A. & Kivshar, Y. S. Spontaneous radiation of a finite-size dipole emitter in hyperbolic media. *Physical Review A—Atomic, Molecular, and Optical Physics* **84**, 023807 (2011).

12 Choi, B. *et al.* Giant Optical Anisotropy in 2D Metal–Organic Chalcogenates. *ACS nano* **18**, 25489-25498 (2024).

13 Zhang, H. *et al.* Cavity-enhanced linear dichroism in a van der Waals antiferromagnet. *Nature Photonics* **16**, 311-317 (2022).

14 Grudinin, D. *et al.* Hexagonal boron nitride nanophotonics: a record-breaking material for the ultraviolet and visible spectral ranges. *Materials Horizons* **10**, 2427-2435 (2023).

15 Wang, H. *et al.* Planar hyperbolic polaritons in 2D van der Waals materials. *Nature communications* **15**, 69 (2024).

16 Ma, W. *et al.* In-plane anisotropic and ultra-low-loss polaritons in a natural van der Waals crystal. *Nature* **562**, 557-562 (2018).

17 Giles, A. J. *et al.* Ultralow-loss polaritons in isotopically pure boron nitride. *Nature materials* **17**, 134-139 (2018).

18 Wang, C. *et al.* Van der Waals thin films of WTe2 for natural hyperbolic plasmonic surfaces. *Nature communications* **11**, 1158 (2020).

19 Wang, F. *et al.* Prediction of hyperbolic exciton-polaritons in monolayer black phosphorus. *Nature communications* **12**, 5628 (2021).

20 Ruta, F. L. *et al.* Hyperbolic exciton polaritons in a van der Waals magnet. *Nature communications* **14**, 8261 (2023).

21 Gershuni, Y. & Epstein, I. In-plane exciton polaritons versus plasmon polaritons: Nonlocal corrections, confinement, and loss. *Physical Review B* **109**, L121408 (2024).

22 Eini, T. *et al.* Electrically tunable interband collective excitations in biased bilayer and trilayer graphene. *Physical Review Letters* **134**, 196903 (2025).

23 Kats, I., Eini, T. & Epstein, I. Monolayer semiconductor superlattices as hyperbolic materials at visible to near-infrared frequencies. *Physical Review B* **111**, L041302 (2025).

24 Dai, S. *et al.* Tunable phonon polaritons in atomically thin van der Waals crystals of boron nitride. *Science* **343**, 1125-1129 (2014).

25 Venturi, G., Mancini, A., Melchioni, N., Chiodini, S. & Ambrosio, A. Visible-frequency hyperbolic plasmon polaritons in a natural van der Waals crystal. *Nature Communications* **15**, 9727 (2024).

26 Watanabe, K., Taniguchi, T. & Kanda, H. Direct-bandgap properties and evidence for ultraviolet lasing of hexagonal boron nitride single crystal. *Nature materials* **3**, 404-409 (2004).

27 Cassabois, G., Valvin, P. & Gil, B. Hexagonal boron nitride is an indirect bandgap semiconductor. *Nature photonics* **10**, 262-266 (2016).

28 Elias, C. *et al.* Flat bands and giant light-matter interaction in hexagonal boron nitride. *Physical Review Letters* **127**, 137401 (2021).

29 Zunger, A., Katzir, A. & Halperin, A. Optical properties of hexagonal boron nitride. *Physical Review B* **13**, 5560 (1976).

30 Tarrio, C. & Schnatterly, S. Interband transitions, plasmons, and dispersion in hexagonal boron nitride. *Physical review B* **40**, 7852 (1989).

31 Cao, X., Clubine, B., Edgar, J., Lin, J. & Jiang, H. Two-dimensional excitons in three-dimensional hexagonal boron nitride. *Applied physics letters* **103** (2013).

32 Arnaud, B., Lebègue, S., Rabiller, P. & Alouani, M. Huge excitonic effects in layered hexagonal boron nitride. *Physical review letters* **96**, 026402 (2006).

33 Wirtz, L., Marini, A. & Rubio, A. Excitons in boron nitride nanotubes: dimensionality effects. *Physical review letters* **96**, 126104 (2006).

34 Caldwell, J. D. *et al.* Sub-diffractional volume-confined polaritons in the natural hyperbolic material hexagonal boron nitride. *Nature communications* **5**, 5221 (2014).

35 Artús, L. *et al.* Ellipsometry study of hexagonal boron nitride using synchrotron radiation: transparency window in the Far-UVC. *Advanced Photonics Research* **2**, 2000101 (2021).

36 Sponza, L. *et al.* Direct and indirect excitons in boron nitride polymorphs: A story of atomic configuration and electronic correlation. *Physical Review B* **98**, 125206 (2018).

37 Fujiwara, H. *Spectroscopic ellipsometry: principles and applications*. (John Wiley & Sons, 2007).

38 Dahal, R. *et al.* Anisotropic charge carrier transport in free-standing hexagonal boron nitride thin films. *Applied physics express* **9**, 065801 (2016).

39 Hoffman, T. B., Clubine, B., Zhang, Y., Snow, K. & Edgar, J. H. Optimization of Ni–Cr flux growth for hexagonal boron nitride single crystals. *Journal of crystal growth* **393**, 114-118 (2014).

40 Scuri, G. *et al.* Large excitonic reflectivity of monolayer MoSe 2 encapsulated in hexagonal boron nitride. *Physical review letters* **120**, 037402 (2018).

41 Epstein, I. *et al.* Near-unity light absorption in a monolayer WS2 van der Waals heterostructure cavity. *Nano letters* **20**, 3545-3552 (2020).

42 Li, M., Biswas, S., Hail, C. U. & Atwater, H. A. Refractive index modulation in monolayer molybdenum diselenide. *Nano Letters* **21**, 7602-7608 (2021).

43 Horng, J. *et al.* Perfect absorption by an atomically thin crystal. *Physical Review Applied* **14**, 024009 (2020).

44 Atash Kahlon, A. *et al.* Importance of pure dephasing in the optical response of excitons in high-quality van der Waals heterostructures. *Physical Review B* **112**, L041402 (2025).

45 Meshulam, M. *et al.* Temperature-Dependent Optical and Polaritonic Properties of Excitons in hBN-Encapsulated Monolayer TMDs. *Advanced Optical Materials* **n/a**, e02535 (2025). https://doi.org:https://doi.org/10.1002/adom.202502535

46 Cannuccia, E., Monserrat, B. & Attaccalite, C. Theory of phonon-assisted luminescence in solids: application to hexagonal boron nitride. *Physical Review B* **99**, 081109 (2019).

47 Paleari, F., PC Miranda, H., Molina-Sánchez, A. & Wirtz, L. Exciton-phonon coupling in the ultraviolet absorption and emission spectra of bulk hexagonal boron nitride. *Physical review letters* **122**, 187401 (2019).

48 Malitson, I. H. Interspecimen comparison of the refractive index of fused silica. *Journal of the optical society of America* **55**, 1205-1209 (1965).

49 Dodge, M. J. Refractive properties of magnesium fluoride. *Applied optics* **23**, 1980-1985 (1984).

50 Reshef, O., De Leon, I., Alam, M. Z. & Boyd, R. W. Nonlinear optical effects in epsilon-near-zero media. *Nature Reviews Materials* **4**, 535-551 (2019).

51 Liberal, I. & Engheta, N. Zero-index structures as an alternative platform for quantum optics. *Proceedings of the National Academy of Sciences* **114**, 822-827 (2017).

52 Hill, H. M. *et al.* Observation of excitonic Rydberg states in monolayer MoS2 and WS2 by photoluminescence excitation spectroscopy. *Nano letters* **15**, 2992-2997 (2015).

53 He, K. *et al.* Tightly bound excitons in monolayer WSe 2. *Physical review letters* **113**, 026803 (2014).

54 Wang, G. *et al.* Exciton states in monolayer MoSe2: impact on interband transitions. *2D Materials* **2**, 045005 (2015).

55 Blancon, J.-C. *et al.* Extremely efficient internal exciton dissociation through edge states in layered 2D perovskites. *Science* **355**, 1288-1292 (2017).

56 Song, B. *et al.* Determination of dielectric functions and exciton oscillator strength of two-dimensional hybrid perovskites. *ACS Materials Letters* **3**, 148-159 (2020).

57 Ishihara, T., Takahashi, J. & Goto, T. Optical properties due to electronic transitions in two-dimensional semiconductors (C n H 2 n+ 1 NH 3) 2 PbI 4. *Physical review B* **42**, 11099 (1990).

58 Jariwala, D., Davoyan, A. R., Wong, J. & Atwater, H. A. Van der Waals materials for atomically-thin photovoltaics: promise and outlook. *Acs Photonics* **4**, 2962-2970 (2017).

59 Ahuja, R. *et al.* Electronic and optical properties of lead iodide. *Journal of applied physics* **92**, 7219-7224 (2002).

60 Li, Y. *et al.* Measurement of the optical dielectric function of monolayer transition-metal dichalcogenides: MoS 2, Mo S e 2, WS 2, and WS e 2. *Physical Review B* **90**, 205422 (2014).

61 Anantharaman, S. B. *et al.* Ultrastrong light–matter coupling in two-dimensional metal–organic chalcogenolates. *Nature Photonics*, 1-7 (2025).

62 Beliaev, L. Y., Shkondin, E., Lavrinenko, A. V. & Takayama, O. Thickness-dependent optical properties of aluminum nitride films for mid-infrared wavelengths. *Journal of Vacuum Science & Technology A* **39** (2021).

63 Chernikov, A. *et al.* Exciton binding energy and nonhydrogenic Rydberg series in monolayer WS 2. *Physical review letters* **113**, 076802 (2014).

64 Epstein, I. *et al.* Highly confined in-plane propagating exciton-polaritons on monolayer semiconductors. *2D Materials* **7**, 035031 (2020).

65 Kats, M. A., Blanchard, R., Genevet, P. & Capasso, F. Nanometre optical coatings based on strong interference effects in highly absorbing media. *Nature materials* **12**, 20-24 (2013).

66 Pettersson, L. A., Roman, L. S. & Inganäs, O. Modeling photocurrent action spectra of photovoltaic devices based on organic thin films. *Journal of Applied Physics* **86**, 487-496 (1999).

67 Peumans, P., Yakimov, A. & Forrest, S. R. Small molecular weight organic thin-film photodetectors and solar cells. *Journal of Applied Physics* **93**, 3693-3723 (2003).

68 Ma, E. Y. *et al.* The reststrahlen effect in the optically thin limit: A framework for resonant response in thin media. *Nano Letters* **22**, 8389-8393 (2022).

69 Basov, D., Fogler, M. & García de Abajo, F. Polaritons in van der Waals materials. *Science* **354**, aag1992 (2016).

70 Jackson, E., Tischler, J., Ratchford, D. & Ellis, C. The role of losses in determining hyperbolic material figures of merit. *Scientific Reports* **14**, 25156 (2024).

71 Novotny, L. & Hecht, B. *Principles of nano-optics*. (Cambridge university press, 2012).

72 Maier, S. A. *Plasmonics: fundamentals and applications*. Vol. 1 (Springer, 2007).

73 Wang, H. *et al.* Strain-Tunable Hyperbolic Exciton Polaritons in Monolayer Black Arsenic with Two Exciton Resonances. *Nano letters* **24**, 2057-2062 (2024).

74 Eini, T., Asherov, T., Mazor, Y. & Epstein, I. Valley-polarized hyperbolic exciton polaritons in few-layer two-dimensional semiconductors at visible frequencies. *Physical Review B* **106**, L201405 (2022).

75 Low, T. *et al.* Polaritons in layered two-dimensional materials. *Nature materials* **16**, 182-194 (2017).

76 Fei, Z. *et al.* Nano-optical imaging of WS e 2 waveguide modes revealing light-exciton interactions. *Physical Review B* **94**, 081402 (2016).

77 Pizzocchero, F. *et al.* The hot pick-up technique for batch assembly of van der Waals heterostructures. *Nature communications* **7**, 11894 (2016).

78 Malitson, I. H. & Dodge, M. J. Refractive index and birefringence of synthetic sapphire. *J. Opt. Soc. Am* **62**, 1405 (1972).

79 McPeak, K. M. *et al.* Plasmonic films can easily be better: rules and recipes. *ACS photonics* **2**, 326-333 (2015).

Editorial Summary

A few anisotropic van der Waals materials have been shown to host hyperbolic polaritons in the visible and infrared ranges. Here, the authors characterize the complex dielectric function of hexagonal boron nitride in the deep-ultraviolet regime, predicting a natural hyperbolic dispersion supporting hyperbolic exciton polaritons.

Peer review information: *Nature Communications* thanks the anonymous reviewers for their contribution to the peer review of this work. A peer review file is available.